Experimental study of a subscale rotating detonation chamber fed with gh2 / go2

Ewen Bard, Wolfgang Armbruster, Rheindorf Kilian, Alexander Bee, Michael Börner, Stephan General, Justin S Hardi, Davidenko Dmitry, Stéphane Boulal, Pierre Vidal

EXPERIMENTAL STUDY OF A SUBSCALE ROTATING DETONATION CHAMBER FED WITH GH2 / GO2

Ewen Bard[(1),(2)], **Wolfgang Armbruster**[(1)], **Kilian Rheindorf**[(1)], **Alexander Bee**[(1)], **Michael Börner**[(1)], **Stephan General**[(1)], **Justin S. Hardi**[(1)], **Dmitry Davidenko**[(2)], **Stéphane Boulal**[(2)], and **Pierre Vidal**[(3)]

[(1)] *DLR - German Aerospace Center, Rocket Propulsion Technology, Institute of Space Propulsion, Hardthausen am Kocher, Germany*
[(2)] *DMPE, ONERA, Université Paris Saclay, F-91123 Palaiseau, France, Email: ewen.bard@onera.fr*
[(3)] *Institut Pprime, CNRS UPR 3346, ENSMA, Futuroscope-Chasseneuil, France*

KEYWORDS: rotating detonation, annular chamber, experiment, image analysis, detonation regime

ABSTRACT

Many aspects are currently under investigation before practical implementation of Rotating Detonation Engines (RDE). A key aspect is the ability to control the detonation regime, which is characterized by the number of wave fronts, their direction of rotation and velocity. The purpose of testing a small-scale rotating detonation chamber (RDC) is to identify the main operation and injection conditions governing the detonation dynamics under various injection conditions at affordable cost. This paper will present the methods used to characterize various detonation regimes obtained during one test run. Dynamic measurements of wall pressure in the chamber and high-speed video recordings are complementary data to evaluate the established regimes of detonation during RDC operation.

1. INTRODUCTION

The last two decades have seen an exponentially growing interest in Rotating Detonation Engines (RDE), also known as Continuous Detonation Wave Engines (CDWE) [1, 2]. The fundamental operating principle of an RDE involves continuous rotation of one or more detonation waves in a mixture of propellants, which are injected in an annular combustor, called Rotating Detonation Chamber or RDC, as shown schematically on Fig. 1.

Experimental, numerical and theoretical studies have been discussing potential benefits of RDEs, such as higher efficiency, compared with quasi-isobaric combustors, and component downsizing due to shorter combustion times [3–7]. These improvements are still under investigation.

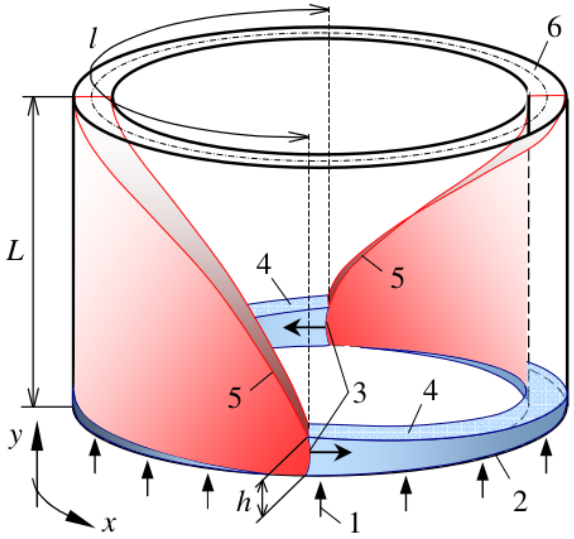

Figure 1: RDE operating principle: (1) propellant injection, (2) injection plane, (3) detonation fronts, (4) fresh mixture layer, (5) oblique shocks attached to the detonations, (6) chamber outlet plane [8].

Experimental techniques to study rotating detonation are now well documented [9–11]. High-speed camera recordings, e.g.[12–16], are commonly implemented, but the large amount of data thus generated over a few hundred milliseconds requires automated post-processing. This paper describes an experimental work on the detonation regimes in an RDC operated with hydrogen (GH2) - oxygen (GO2) mixtures. The analysis uses an implementation of the image processing method of Bennewitz et al. [17, 18] and is cross-checked with unsteady pressure evolution recorded at the RDC wall.

2. RDE EXPERIMENTAL SETUP

The first subsection describes the RDC geometry and the initiation method, the second the pressure and mass flow rate measurement techniques, and the third the high-speed visualization conditions.

2.1. RDC model geometry

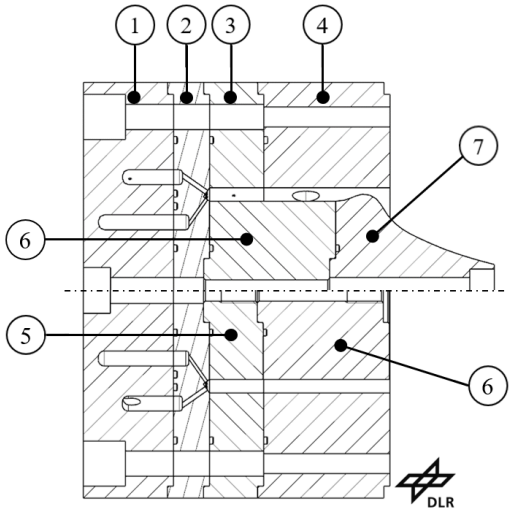

Figure 2: Sub-scale RDC model with a chocking plug on the top and without throat in the bottom: (1) Manifold plate, (2) Injector plate, (3) Measurement ring, (4) Ignition ring, (5) Core cylinder, short, (6) Core cylinder, long, (7) Throat plug

Figure 2 shows the sub-scale RDC. The manifold plate (1) consists of two separate annular plenums. Gaseous propellants are fed in the chamber through an injector plate (2) in the "unlike doublet" configuration, e.g. (Ref), to form a fresh mixture layer. The plate has 72 pairs of normal impinging orifices inclined from the axial direction at: 35° for oxygen and 55° for hydrogen. The orifice diameters are 1 mm and 1.5 mm for GO2 and GH2, respectively. The RDC outer wall is made up of the measurement ring (3) and the ignition ring (4). The chamber outer diameter is 68 mm. The length from the injection plane to the combustor outlet is 60 mm. The setup then has two configurations. The first one (Fig. 2, bottom) includes the center bodies (5) and (6) which are 59 mm diameter plain cylinders constituting the inner wall of the chamber, so the RDC width is 4.5 mm. The second one (Fig. 2, top) includes the center body (6) – but not the (5) – and a sonic throat (7) with a 50 % cross-sectional restriction. Parts (2) to (7) are made of a plain copper alloy which, acting as a heat sink, enables short test duration of approximately 0.7 seconds.
The detonation is initiated using a classical predetonator, here implemented as a 4 mm diameter tube connected to the RDC outer wall at the ignition ring (2), using GH2-GO2 as the driver.

2.2. Pressure and flow rate measurements

Three KISTLER 603-A pressure sensors, implemented at the sampling rate of 2 MHz, were flush mounted with the RDC outer wall on the measurement ring (3) (Fig. 3) with the angle of 135° between P1 and P2 and between P2 and P3. The axial distance of the sensors to the injection plane was 8 mm. Figure 8-top shows a typical pressure signal.

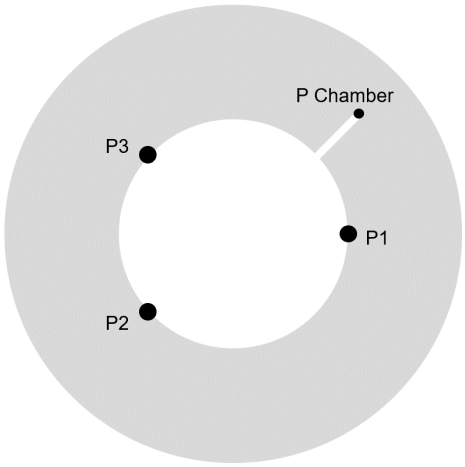

Figure 3: Locations of the different transducers in the measurement ring 8 mm downstream from the injection plane

The pressure was also measured using four KISTLER 4043A sensors implemented at the sampling rate of 10 kHz, one at the manifold ring for each propellant, and two within the combustion chamber at 8 and 38 mm downstream from the injection plane. Figures 4 shows an example of pressure evolution recording.

The propellant mass flow rates were measured using two Coriolis flowmeters sampled at 100 Hz mounted in the feeding lines. Mass flow rates of $\sim$ 70 g/s, i.e. mass flux of $\sim$ 80 kg/m²/s, were found sufficient to achieve rotating detonation regimes using GH2-GO2 in the RDC described above. In most tests, the mixture ratio ROF $= \dot{m}_{O_2}/\dot{m}_{H_2}$ was maintained below the stoichiometric value, i.e. 5 $<$ ROF $<$ 8, to prevent the hardware oxidation, but a few tests were conducted with oxidizer-rich conditions, i.e. ROF $\sim$ 9. Figure 5 and 6 show example of mass flow rates and ROF conditions during test.

2.3. High-speed video recording

A Photron SA-Z high-speed camera, positioned seven meters downstream away from the RDC outlet, was implemented at a frame rate of 180 kHz and the resolution of 256 x 256 pixels, resulting in approximately 200 x 200 pixels over the annulus area. No specific emission filter is used.

3. REFERENCE TEST CONDITIONS

The configuration used for the test described below is the straight RDC chamber (Fig. 2, bottom). The mass flow rates of $\dot{m_{O_2}}$ and $\dot{m_{H_2}}$ could be varied during the test run. Figure 4 shows the evolution of the static pressure recorded in the propellant plenums and in the combustion chamber for the conditions of mass flow rates and mixture ratio on Figures 5 and 6.

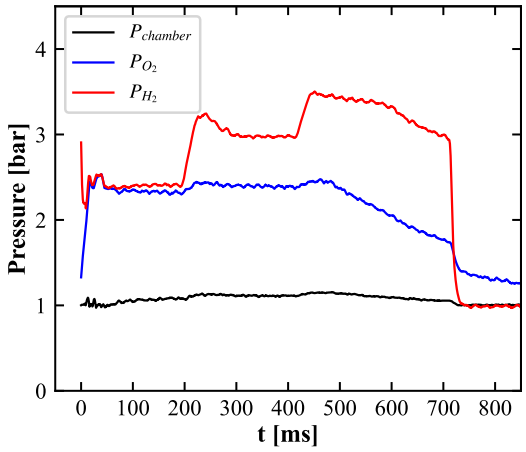

Figure 4: Pressure evolution in the propellant plenums and the combustion chamber

The Coriolis flowmeters require the rates to be corrected. Reason for that is their low sampling rate and the distance between their installation place and the injectors. The discharge coefficient C_d of each injector is calculated over the most stabilized part of the Coriolis measurement curve

$$C_d = \frac{\dot{m}}{A\sqrt{2\rho\Delta P}}, \qquad \text{Eq.1}$$

where ΔP is the pressure difference between the manifold plenums and the chamber, A is the cross-sectional injector area and ρ the gas density. Figure 5 shows the corrected mass flow rates. The total mass flow rate $\dot{m}_{total}$ varies from 48 to 53 g/s and decreases to 38 g/s during the closing of the oxygen valve. The manifold pressures of the propellants are controlled to run with different mixture ratios ROF during the test, following a step-shaped profile (Fig.6). This ratio was varied from close to stoichiometry ($ROF_{st} = 7.94$) to rich ($ROF \gtrsim 4.8$).

4. IMAGE PROCESSING METHOD

This processing method [17, 18] aims to circumvent the shortcoming due to time-averaging inherent in the Dynamic Mode Decomposition (DMD) [19], a modal decomposition technique commonly used to study periodic phenomena in fluid dynamics. However, DMD results may be ambiguous when

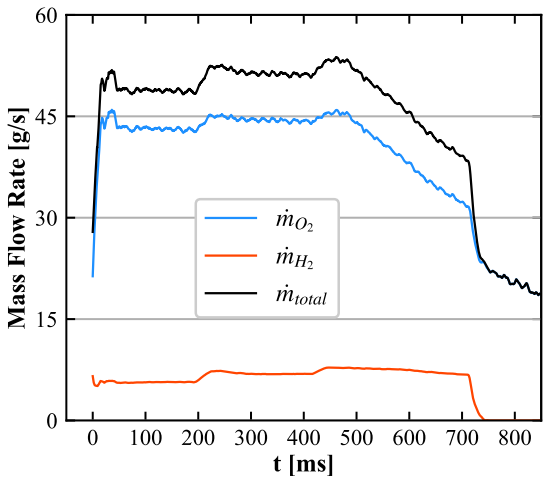

Figure 5: Evolution of the GO2 and GH2 mass flow rates

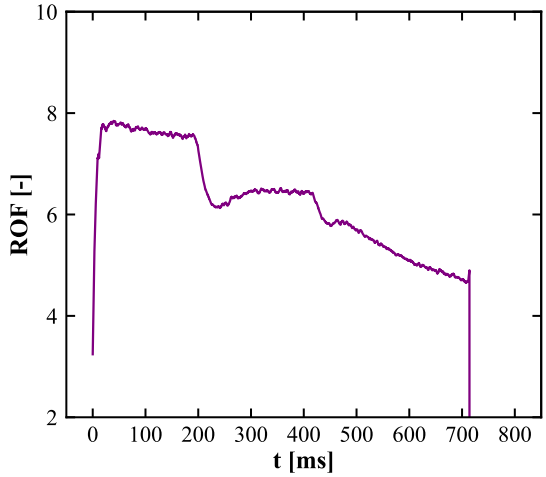

Figure 6: Evolution of the mixture ratio (ROF)

applied to the wave dynamics in RDCs due to unsteady phenomena involving detonation onset or failure, and changes in wave propagation direction. The algorithm automates the determination of the number, the rotation direction and the frequency of the wave fronts.

In our conditions, the high-speed camera recording is segmented into intervals of 500 frames, a number that was found to provide a satisfying compromise between the accuracy of the results and a reasonable processing time. The first step was an image correction which included subtracting the mean image and adjusting the brightness with a correction factor to emphasize the detonation wave fronts (Fig.7). The second step is to locate the chamber annulus by conducting a pixel-wise FFT and extract the areas with highest oscillation amplitudes which correspond to frequencies for an expected range of wave front numbers. These pixels are then used to detect the wave trajectories based on a Taubin fit [20]. The combustor annulus is next conveniently di-

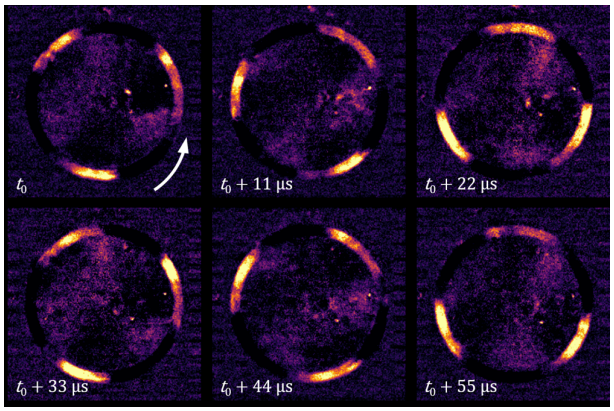

Figure 7: Three-wave mode of detonation with enhanced contrast [21]

vided into 360 bins. Figure 8 (bottom) shows an example of the angular position θ as a function of time t diagram obtained after post-processing. Each point is colored according to the average luminescence evaluated in one bin at a given time.

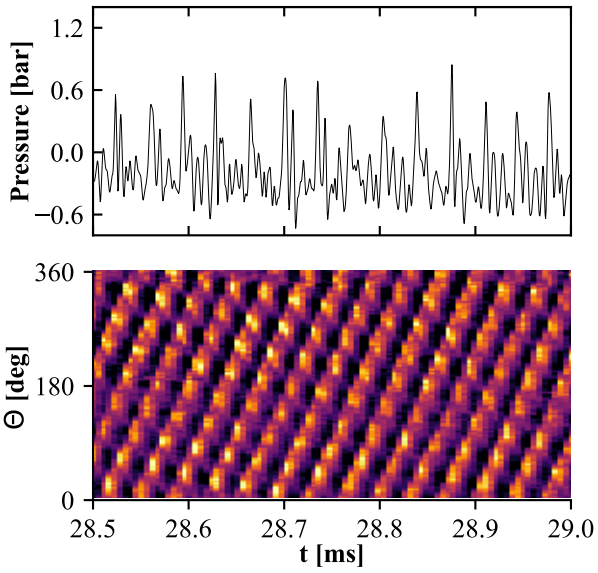

Figure 8: Synchronized pressure evolution (top, sensor P1) and wave front angular position in a 3 co-rotating mode (bottom)

The final step consists in a 2D-FFT analysis on the θ - t matrix. This analysis reveals periodic modes in both temporal and angular coordinates, which highlights the wave number and corresponding rotation frequency and direction. Figure 9 shows the resulting $N_w - f$ diagram for the time interval 27 - 28 ms. Negative sign of N_w corresponds to the counterclockwise rotation direction, and a positive sign to the clockwise direction.

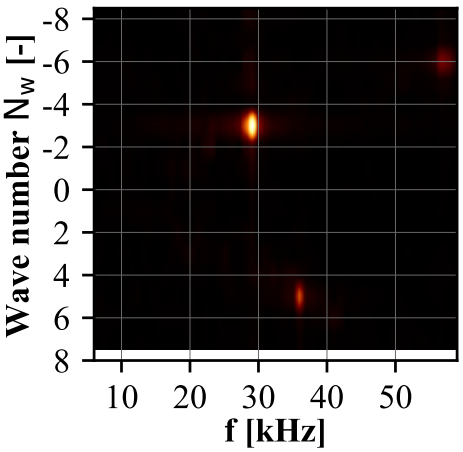

Figure 9: Number of wave fronts and rotation frequency from the 2D-FFT analysis of the diagram on Fig.8, bottom

We have applied this implementation to various RDC experiments, providing data on the wave number N_w, the rotation direction and frequency f, and thus deriving the tangential wave velocity U_D

$$U_D = \frac{\pi d_{\text{out}} f}{N_w}, \qquad \text{Eq.2}$$

where d_{out} is the annulus outer diameter.

5. TEST RUN ANALYSIS

5.1. Detonation regime

The processing algorithm is reproduced over the whole test duration to isolate stable regimes and detect regime changes. Since the results mostly showed a counter-rotating regime [21], i.e., two groups of waves rotating in opposite directions, the $N_w - f$ diagram often showed two or more bright points of nearly the same intensity. Figure 9 shows the case of two bright points, one indicating a regime corresponding to ∼28 kHz and 3 waves rotating in the counterclockwise direction (negative wave number) and another at 35 kHz and 5 waves in the clockwise direction (positive wave number). To decide whether or not a secondary mode is physically valid, an empirical criterion was defined as follows: if the intensity of the secondary mode detected by the algorithm reaches more than 50% of the most intense one, then it is considered as an physical mode. Different values of the criterion threshold have been tested and the 50% threshold appeared to be the most suitable.

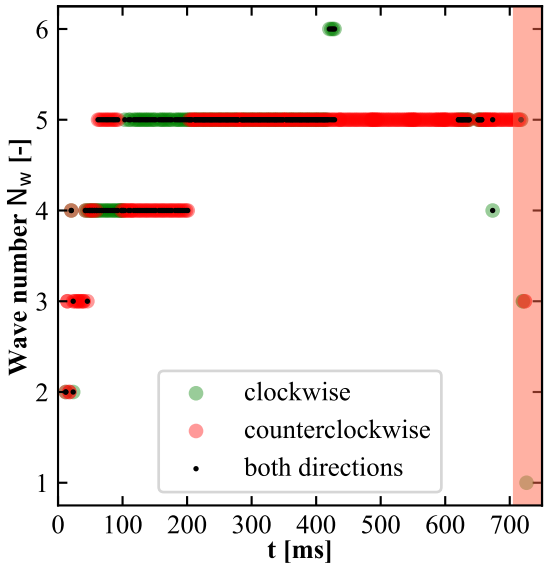

Figure 10: Evolution of the number of waves occurring in the RDC during the test run as defined by the image processing method with a 50% threshold

Fig.10 shows the wave numbers detected during the test run. The point colors correspond to the wave rotation direction. The black dot indicates both clockwise (green) and counter-clockwise (red) rotation directions in the same interval, i.e. if the black dot is shown in one circle, then an opposite rotating mode exists. When both rotation modes have the same N_w, then the green and red circles overlap and change to a dark-red tone, such as in the interval 210 < t < 400 ms, where the algorithm identified 5 pairs of counter-rotating waves. As to the dynamics of the detonation waves during the test run, many observations can be made from the diagram on Fig.10. The test features a complex transient phase, within the interval 0 < t < 210 ms. During the first 80 ms, the detonation regime varied from counter-rotating waves (2 - 2 mode), 3 co-rotating waves, then to 3 - 3 and also 4 - 4 counter-rotating modes. During the interval 80 < t < 200 ms, asymmetrical modes are observed with 4 and 5 counter-rotating waves (4 - 5 mode) in the opposite direction. This mode switched to 5 - 4 mode at $t \sim$ 90 ms. Between 200 ms and 430 ms, 5 counter-rotating waves are observed in the chamber. For 430 < t < 615 ms, 5 co-rotating waves stabilize. Finally the red area at the end of the test interval indicates that the results of the image analysis are varying too much to make valid observations.

5.2. Wall pressure dynamics

High-frequency recordings of the wall pressure inside the RDC, e.g. Fig.8, can be represented in the form of a spectrogram, e.g. Fig.11. It was computed with a frequency resolution of 400 Hz, a window length of 8192 points per segment and 4096 points overlapping between segments [22, 23].

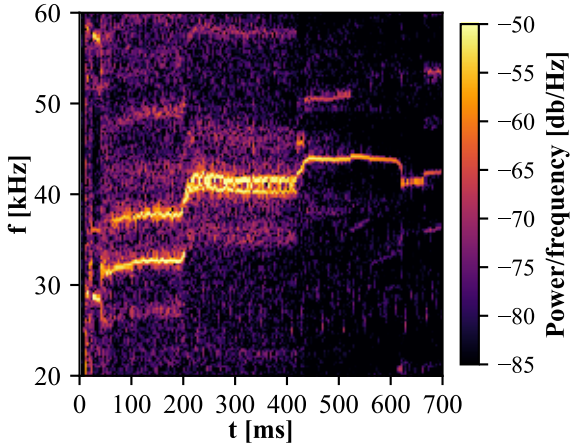

Figure 11: Spectrogram of the pressure - t signal on Fig. 8, (top) over the whole test duration

The dominant mode frequencies are indicated by the highest intensity in the spectrogram. Several transitions between quasi-steady phases are observed when the dominant mode frequency changes abruptly. These phases correspond to the several detonation regimes indicated by the diagram on Fig.10. For example, there are two co-existing dominant frequencies for 70 < t < 200 ms. Then a 20 ms transition phase leads to another stable phase with two dominant frequencies for 220 < t < 410 ms. Finally, for 450 < t < 600 ms, a single-frequency regime establishes.

5.3. Wave propagation velocity

Figure 12 shows the evolution of the wave velocity resulting from the image processing analysis (see Sect. 4). A general good agreement is found between the two measurement techniques: the transition times and quasi-steady phases on Fig.12 match those on Fig.11.The first observation is that detonation velocities ranging from 1600 m/s to more than 2200 m/s were achieved during this test. Another important trend is that the co-rotating modes of detonation (points without black dot) have higher velocities than the corresponding counter-rotating modes (points with black dot) with the same number of waves in a group. This will be further discussed in Sect. 6. It is worth mentioning that the dominant frequencies determined by both measurement techniques differ by 0.42 %, i.e. a difference in the detonation velocity of only 8.5 m/s.

Load Point	R 1	R 2	R 3	R 4
Mass flow rate [g/s]	51.35	48.8	51.47	[53.3 - 44]
ROF	7.77	7.58	6.4	[5.8 - 5]
Wave mode	3	4 - 5	5 - 5	5
Wave velocity [m/s]	2029.5	1742.1 - 1615	1773.1 - 1700	1884.6
Ratio U_D / D_{CJ} [%]	71	60.5 - 55.8	58.7 - 53.2	[60.8 - 58.4]

Table 1: Regimes and their corresponding interval averaged main parameters

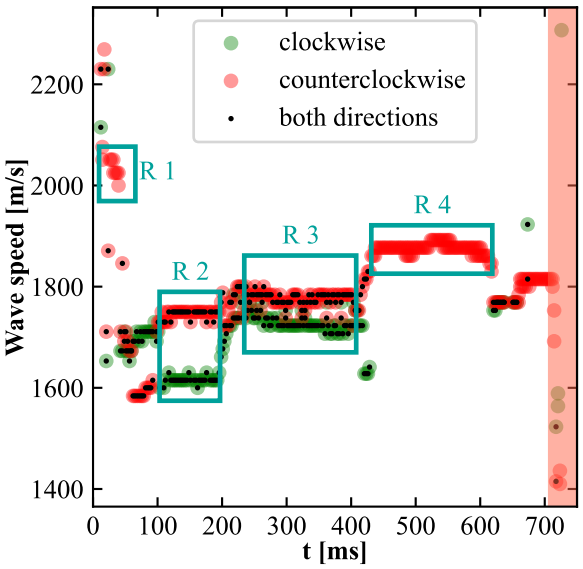

Figure 12: Test run analysis : Wave speed over time

We now describe the four types of regimes obtained during the test run. Figure 13 collectively shows the $\theta - t$ and $N_w - f$ diagrams associated to each regime. Table 1 summarizes the observed conditions and detonation wave velocities over the four different regimes presented above.

The first one (Regime 1 on Fig.12, here after referred to as "R") featured 3 co-rotating waves. It was obtained during the interval 25 < t < 40 ms. The $\theta - t$ and $N_w - f$ diagrams are shown on Fig.13 (a). This mode corresponds to a dominant frequency of 28.6 kHz, which corresponds to a detonation velocity $U_D \approx$ 2030 m/s. The ideal Chapman-Jouguet (CJ) velocity was evaluated to $D_{CJ} =$ 2859.4 m/s using the NASA CEA computer program for ideal detonation products [24]. The thermodynamic parameters for detonation calculation are : $P_0 =$ 1 bar, $T_0 =$ 285 K, hydrogen as fuel reactant, the equivalence ratio Φ = ROF_{st} / ROF = 7.94 / ROF which was averaged over the regime interval and reactants injection temperatures $T_{fuel} = T_{oxidizer} =$ 285 K. This gives a detonation velocity relative to the CJ velocity of 71%.

The second regime (R 2), obtained for 100 < t < 200 ms, featured 5 waves rotating clockwise and 4 waves rotating counter-clockwise. Each group of waves propagate at a velocity of 1615 and 1742 m/s respectively. Figure 13 (b) shows 5 and 4 wave fronts intersecting each other. The dominant frequencies are 37.8 kHz and 32.7 kHz respectively.

The third regime (R 3), observed for 200 $< t <$ 400 ms, featured 5 co-rotating and 5 counter-rotating waves. During this phase, the counterclockwise rotating waves are still propagating at a higher velocity than the clockwise rotating waves, at about 1775 m/s and 1725 m/s, respectively. On Fig.13 (c, left), we note that the intersection points are staying on a horizontal line, compared to Fig.13 (b, left) where they were slightly descending over time since the regime was unsymmetrical.

Finally, for the interval $\sim$ 430 $< t <$ $\sim$ 610 ms, 5 co-rotating waves (R 4) stabilized at a velocity of roughly 1885 m/s. This is a unexpected observation since this quasi-steady regime is obtained while both the mass flow rate and ROF are strongly decreasing (see Figs. 4 to 6). In particular, the ROF dropped from 5.8 to 4.6. Fig. 13 (d) shows the corresponding fronts and frequency of operation.

(a) 3 co-rotating waves - R1

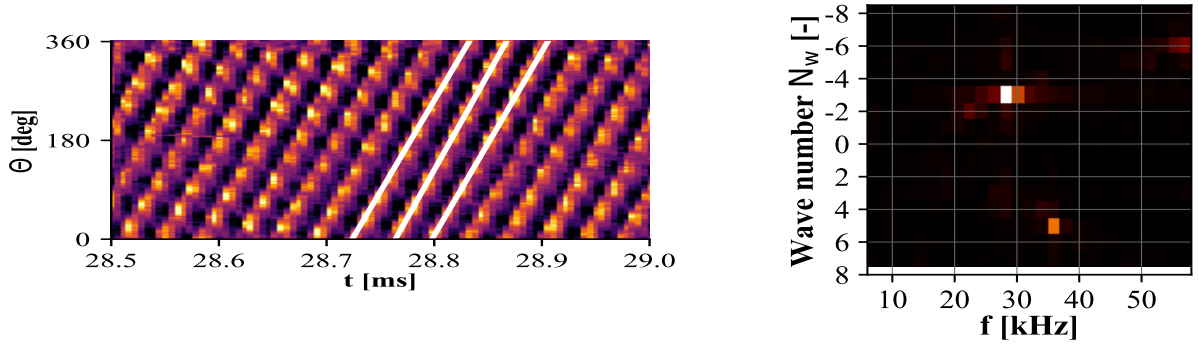

(b) 4 VS 5 counter-rotating waves - R2

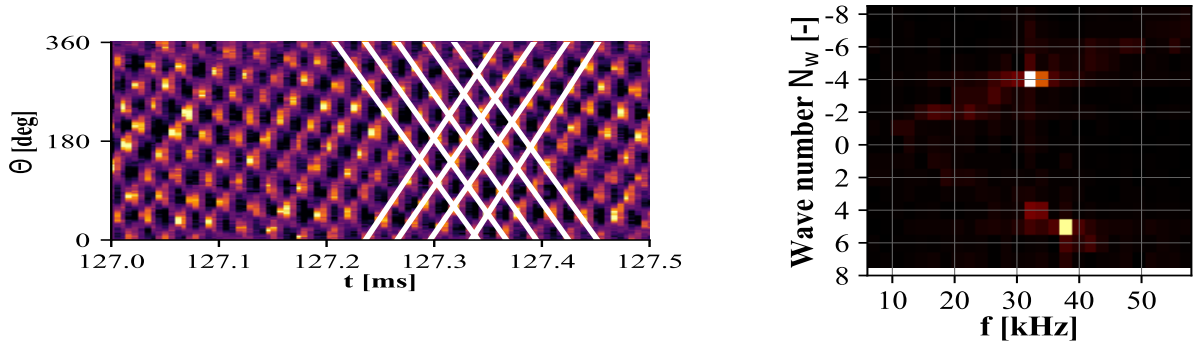

(c) 5 VS 5 counter-rotating waves - R3

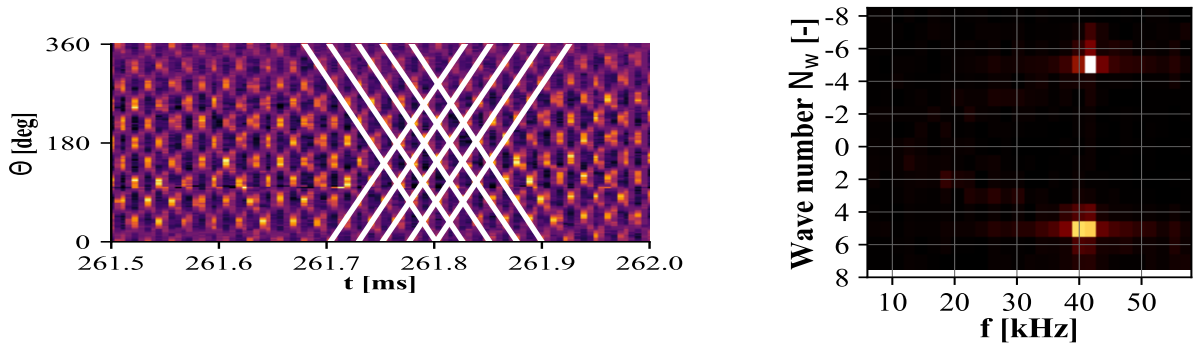

(d) 5 co-rotating waves - R4

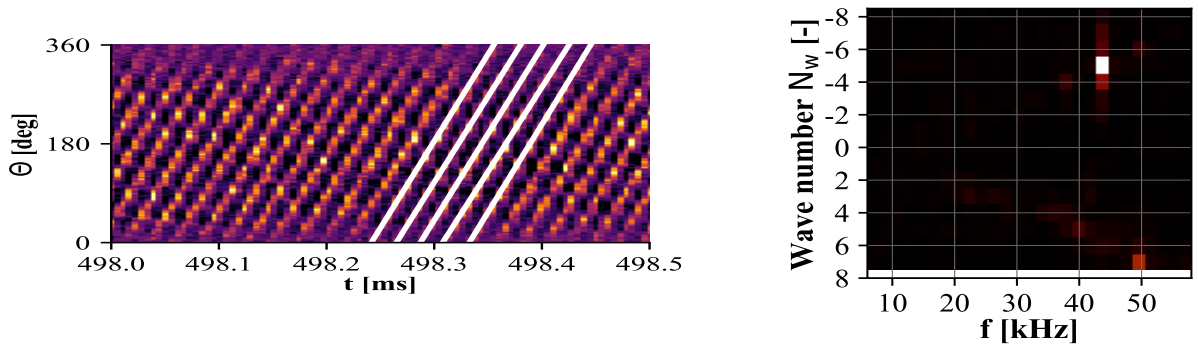

Figure 13: θ - t (left panel) and N_w - f (right panel) diagrams for different detonation regimes observed during the test run

6. DISCUSSION

Counter-rotating modes are less interesting than co-rotating ones because they correspond to less efficient combustion. They are characterized by variations in the wave intensity between collisions, which produce a strong local impact on the injector operation. However, understanding the mechanisms that drive the evolution from one regime to another with regard to the injection physical parameters (mass flow rate, mixture ratio, fluid velocity at the injection) brings knowledge to the characterization of the propellant mixing efficiency given an injector. Open questions are:

- How to explain the stable asymmetrical regime with 4 - 5 counter-rotating waves? Could this interpretation result from the setup of the image processing method?
- What could be the explanation for a difference in the wave velocities in the regime with 5 - 5 counter-rotating waves, since it is a symmetric mode?
- Which physical parameter of the injection could be the leading factor controlling the regime changes? For example, why did the mass-flow rate ramping down seem to have triggered a transition from 5 - 5 counter-rotating waves to 5 co-rotating waves?

These questions will be addressed by testing further parameter ranges in upcoming campaign and CFD simulations.

7. CONCLUSION

This paper presents and analyses experimental results for a model RDE combustor operated with gaseous hydrogen and oxygen. Dynamic measurements of wall pressure and high-speed video recordings allows determination of the most favorable conditions for the detonation propagation and the most efficient regimes of RDC operation. Based on an image processing method [17, 18] that circumvent the shortcoming due to time-averaging inherent in the Dynamic Mode Decomposition (DMD) [19], different detonation regimes are identified. Three and five co-rotating wave modes show higher rotation velocities than the corresponding counter-rotating modes. The implemented techniques will help to analyse other test runs and to obtain RDC model characteristics in a wide range of conditions. The data will be used in CFD simulations to further evaluate the RDE efficiency and loss factors.

8. REFERENCES

1. B. V., V. *Stationary spin detonation* in *Soviet Journal of Applied Mechanics and Technical Physics* (1960), 157–164.
2. Cullen, R. E., Nicholls, J. A. & Ragland, K. W. Feasibility Studies of a Rotating Detonation Wave Rocket Motor. *Journal of Spacecraft and Rockets* **3,** 893–898. https://api.semanticscholar.org/CorpusID:123066550 (1966).
3. Wolański, P. Detonative propulsion. *Proceedings of the Combustion Institute* **34,** 125–158. ISSN: 1540-7489. https://www.sciencedirect.com/science/article/pii/S1540748912004014 (2013).
4. Xie, Q. *et al.* Review on the Rotating Detonation Engine and It's Typical Problems. *Transactions on Aerospace Research* **2020,** 107–163. https://doi.org/10.2478/tar-2020-0024 (2020).
5. Shaw, I. J. *et al.* in *Direct Numerical Simulations* (ed Rao, S.) chap. 7 (IntechOpen, Rijeka, 2019). https://doi.org/10.5772/intechopen.90470.
6. Le Naour, B., Davidenko, D., Gaillard, T. & Vidal, P. in *Front. Aerosp. Eng. volume 2* (ed Simone Salvadori Polytechnic University of Turin, I.) (Front. Aerosp. Eng. 2:1152429, 2023).
7. Wolanski, P. Detonation engines. *Journal of KONES Powertrain and Transport* **18,** 515–521 (Jan. 2011).
8. Davidenko, D., Gökalp, I. & Kudryavtsev, A. N. *Numerical simulation of the continuous rotating hydrogen-oxygen detonation with a detailed chemical mechanism* in *West-East High-Speed Flow Field Conference* (2007).
9. Bykovskii, F. A., Zhdan, S. A. & Vedernikov, E. F. Continuous Spin Detonations. *Journal of Propulsion and Power* **22,** 1204–1216. eprint: https://doi.org/10.2514/1.17656. https://doi.org/10.2514/1.17656 (2006).
10. Bykovskii, F., Zhdan, S. & Vedernikov, E. Continuous spin detonation of hydrogen-oxygen mixtures. 1. Annular cylindrical combustors. *Combust Explos Shock Waves 44,* 150–162 (2008).
11. Falempin, F., Le Naour, B. & Miquel, F. *Recent experimental results obtained on Continuous Detonation Wave Engine* in *17th AIAA International Space Planes and Hypersonic Systems and Technologies Conference* (Apr. 2011). ISBN: 978-1-60086-942-6.

12. Bohon, M. D., Orchini, A., Bluemner, R., Paschereit, C. O. & Gutmark, E. J. Dynamic mode decomposition analysis of rotating detonation waves. *Shock Waves* **31,** 637–649. https://api.semanticscholar.org/CorpusID:208254451 (2020).

13. Koch, J., Kurosaka, M., Knowlen, C. & Kutz, J. N. Mode-locked rotating detonation waves: Experiments and a model equation. *Phys. Rev. E* **101,** 013106. https://link.aps.org/doi/10.1103/PhysRevE.101.013106 (1 Jan. 2020).

14. Chacon, F. & Gamba, M. *Detonation Wave Dynamics in a Rotating Detonation Engine* in *AIAA Scitech 2019 Forum* (Jan. 2019).

15. Nakata, K. *et al.* Experimental investigation of inner flow of a throatless diverging rotating detonation engine. *Proceedings of the Combustion Institute* **39,** 3073–3082. ISSN: 1540-7489. https://www.sciencedirect.com/science/article/pii/S1540748922004126 (2023).

16. Hansmetzger, S., Zitoun, R. & Vidal, P. A study of continuous rotation modes of detonation in an annular chamber with constant or increasing section. *Shock Waves* **28,** 1065–1078 (2018).

17. Bennewitz, J., Bigler, B., Hargus, W., Danczyk, S. & Smith, R. *Characterization of Detonation Wave Propagation in a Rotating Detonation Rocket Engine using Direct High-Speed Imaging* in *The Review of scientific instruments* (July 2018).

18. Bennewitz, J., Bigler, B., Schumaker, S. & Hargus, W. J. *Automated image processing method to quantify rotating detonation wave behavior* in *The Review of scientific instruments* (2019), 90(6).

19. Schmid, P. & Sesterhenn, J. Dynamic Mode Decomposition of numerical and experimental data. *Journal of Fluid Mechanics* **656** (Nov. 2008).

20. Taubin, G. Estimation of Planar Curves, Surfaces, and Nonplanar Space Curves Defined by Implicit Equations with Applications to Edge and Range Image Segmentation. *Pattern Analysis and Machine Intelligence, IEEE Transactions on* **13,** 1115–1138 (Dec. 1991).

21. Armbruster, W. *et al. Experimental Investigation of a Small-Scale Oxygen-Hydrogen Rotating Detonation Rocket Combustor* in *AIAA SCITECH 2024 Forum* (AIAA, 2024). eprint: https://arc.aiaa.org/doi/pdf/10.2514/6.2024-2612. https://arc.aiaa.org/doi/abs/10.2514/6.2024-2612.

22. Oppenheim, A. V., Schafer, R. W. & Buck, J. R. *Discrete-Time Signal Processing* Second (Prentice-hall Englewood Cliffs, 1999).

23. Virtanen, P. *et al.* SciPy 1.0: Fundamental Algorithms for Scientific Computing in Python. *Nature Methods* **17,** 261–272 (2020).

24. Gordon, S. & McBride, B. *Computer program for calculation of complex chemical equilibrium compositions and applications, I. Analysis (Ref. 1311)* tech. rep. (NASA, 1994).